FIG. 4 The calculated electronic band structure of the *Pnma* structure of solid hydrogen at 260 GPa. The calculations were performed with a numerical basis set augmented with localized *p*-type orbitals. A total of 163 *k*-points were used in the Brillouin zone integration[29].

1. Mao, H-K & Hemley, R. J. *Rev. mod. Phys.* **66**, 671–692 (1994).
2. Chakravarty, S., Rose, J. H., Wood, D. & Ashcroft, N. W. *Phys. Rev.* B**24**, 1624–1635 (1981).
3. Min, B. I., Jansen, H. J. F. & Freeman, A. J. *Phys. Rev* B**33**, 6383–6390 (1986).
4. Barbee, T. W., Garcia, A., Cohen, M. L. & Martins, J. L. *Phys. Rev. Lett.* **62**, 1150–1153 (1989).
5. Chacham, H. & Louie, S. G. *Phys. Rev. Lett.* **66**, 64–67 (1991).
6. Garcia, A., Barbee, T. W., Cohen, M. L. & Silvera, I. F. *Europhys. Lett.* **13**, 355–360 (1990).
7. Kaxiras, E., Broughton, J. & Hemley, R. J. *Phys. Rev. Lett.* **67**, 1138–1141 (1991).
8. Nagara, H. & Nakahara, T. *Phys. Rev. Lett.* **68**, 2468–2471 (1992).
9. Natoli, V., Martin, R. M. & Ceperley, D. *Phys. Rev. Lett.* **74**, 1601–1604 (1995).
10. Mao, H. K. *et al. Science* **239**, 1131–1134 (1988).
11. Hemley, R. J., Soos, Z. G., Hanfland, M. & Mao, H-K. *Nature* **369**, 384–387 (1994).
12. Car, R. & Parrinello, M. *Phys. Rev. Lett.* **55**, 2471–2474 (1985).
13. Surh, M. P., Barbee, T. W. & Mailhot, C. *Phys. Rev. Lett.* **70**, 4090–4093 (1993).
14. Marx, D. & Parrinello, M. *Z. Phys.* B**95**, 143–144 (1994).
15. Sharma, S. K., Mao, H. K. & Bell, P. M. *Phys. Rev. Lett.* **44**, 886–888 (1980).
16. Hemley, R. J. & Mao, H. K. *Phys. Rev. Lett.* **61**, 857–860 (1988).
17. Hanfland, M., Hemley, R. J., Mao, H. K. & Williams, G. P. *Phys. Rev. Lett.* **69**, 1129–1132 (1992).
18. Hanfland, M., Hemley, R. J. & Mao, H. K. *Phys. Rev. Lett.* **70**, 3760–3763 (1993).
19. Kaxiras, E. & Broughton, J. *Comput. Mater. Sci.* **3**, 368–376 (1995).
20. Hoffmann, R. *Solids and Surfaces* (VCH, New York, 1988).
21. Albright, T. A., Burdett, J. K. & Whangbo, M-H. in *Orbital Interactions in Chemistry* (Wiley, New York, 1985).
22. Hohl, D. *et al. Phys. Rev. Lett.* **71**, 541–544 (1993).
23. Vanderbilt, D. *Phys. Rev.* B**41**, 7892–7895 (1990).
24. Wijngaarden, R. J., Lagendijk, A. & Silvera, I. F. *Phys. Rev.* B**26**, 4957–4961 (1982).
25. Perdew, J. P. & Zunger, A *Phys. Rev.* B**23**, 5048–5078 (1981).
26. Perdew, J. P. *Phys. Rev.* B**33**, 8822–8824 (1986).
27. Becke, A. D. *Phys. Rev.* B**38**, 3098–3100 (1988).
28. Hemley, R. J. *et al. Phys. Rev.* B**42**, 6458–6470 (1990).
29. te Velde, G. & Baerends, E. J. *Phys. Rev.* B**44**, 7888–7903 (1991).

first symmetric (S) orbital in the bonding set are stabilized but the effect on the asymmetric (A) 'non-bonding' orbital is small. However, the highest occupied symmetric orbital will be destabilized and the orbital energy shifted upwards due to out-of-phase interactions between the component orbitals. In the empty orbital set, the first unoccupied asymmetric orbital will decrease in energy because of the favourable in-phase interactions between the molecules. The other two remaining empty orbitals are expected to shift to higher energy owing to increased anti-bonding interactions. The empty asymmetric anti-bonding orbital that is shifted to lower energy can then efficiently interact with the occupied asymmetric 'non-bonding' orbital. The net effect is the destabilization of the central hydrogen molecule due to the increase in the anti-bonding character resulting in a donation of charge density from the two peripheral hydrogen molecules to the central one, forming a weak charge-transfer complex. Consequently, the bond of the central hydrogen lengthens relative to the other two hydrogens which are equivalent by symmetry. The small charge transfer creates a dipole moment in the shorter-bonded hydrogen molecules leading to the enhancement in the infrared absorptivity. In contrast, the longer-bonded hydrogen molecule becomes slightly negatively charged. Owing to crystal reflection symmetry, this molecule cannot possess a permanent dipole moment and hence the stretching vibration will only be Raman-active and the stretching frequency is expected to be lower. The observation of a new Raman band at low frequency at 160 GPa can be attributed to this effect.

We calculate an indirect band gap of 1.4 eV at 260 GPa for this structure (Fig. 4). Thus, even at this pressure (which is considerably higher than experiments have yet reached), we predict that solid hydrogen will remain non-metallic. The Fermi level is located along the Z→Y line and the bottom of the conduction band is at the R point. (Here the letters represent symmetry points on the surface of the first Brillouin zone. At the Y point, the Bloch crystal orbital is destabilized owing to the out-of-phase interactions of the highest occupied symmetric MOs of the molecular fragments whereas at the R point, the crystal orbital is stabilized by the out-of-phase combination of the first empty asymmetric MOs of the molecular fragments. Eventual metallization through the closure of the band gap is likely to occur at these symmetry points at a higher pressure. ☐

Experimental confirmation of universality for a phase transition in two dimensions

C. H. Back, Ch. Würsch, A. Vaterlaus, U. Ramsperger, U. Maier & D. Pescia

Laboratorium für Festkörperphysik der ETH Zürich, CH-8093 Zürich, Switzerland

WHEN a system is poised at a critical point between two macroscopic phases, it exhibits dynamical structures on all available spatial scales, even though the underlying microscopic interactions tend to have a characteristic length scale. According to the universality hypothesis[1,2], diverse physical systems that share the same essential symmetry properties will exhibit the same physical behaviour close to their critical points[1,3–5]; if this is so, even highly idealized models can be used to describe real systems accurately. Here we report experimental confirmation that the scaling behaviour of thermodynamic variables predicted by the universality hypothesis holds over 18 orders of magnitude. We show that the equation of state of a two-dimensional system (an atomic layer of ferromagnetic iron deposited on a non-magnetic substrate) closely follows the behaviour[6] of the two-dimensional Ising model[7]—the first and most elementary statistical model of a macroscopic system with short-range interactions[3].

We grow epitaxial Fe films at room temperature on top of a non-magnetic single-crystal W(110) surface. Pressure in the vacuum chamber during growth does not exceed 2×10^{-10} mbar. In the ferromagnetically ordered phase, the films have a uniaxial easy magnetization axis along the in-plane [1$\bar{1}$0] direction. Along this direction the magnetization M versus applied field H follows a square hysteresis loop, that is, within experimental uncertainty ($< 1\%$) M at $H = 0$ coincides with the value for M in an applied magnetic field. Accordingly[8], such films are in a single domain state. M is measured by means of the magneto-optic Kerr effect[9].

As revealed by our scanning tunnelling microscopy study of the epitaxial growth, films between 1 and 2 atomic layers (AL) consist of one complete AL of Fe followed by a two-dimensional

(2D) network of irregular patches, (Fig. 1). Some third layer is already visible. Low-energy electron diffraction shows, in this thickness range, a sharp $p(1 \times 1)$ pattern indicating growth in registry with the substrate.

In the vicinity of the critical point $[t = (T/T_c - 1), H] = [0, 0]$ the critical exponents β and δ for the zero-field magnetization curve $M(t, H = 0) \propto (-t)^\beta$ and for the critical isotherm $M(H, t = 0) \propto H^{1/\delta}$ are determined to be 0.13 ± 0.02 and 14 ± 5 respectively, (Fig. 2). The theoretical 2D Ising values are $\beta = 1/8$ (exactly known[10]) and $\delta = 15$ (conjectured from numerical calculations[11]).

The sharpness of the transition observed in Fig. 2 is consistent with the magnetic correlation length reaching values of $\sim 1,000$ nm (ref. 9). Evidently, the observed morphological defects—such as monatomic steps arising from the imperfect substrate (typical separation, 50–200 nm in the present sample) and the steps due to patches formation (Fig. 1) during growth—are not able to break the correlation length, that is, the correlations extend to much larger length than the spacing between defects. The picture emerging by comparing Fig. 1 and Fig. 2 is one where locally the number of coexisting layers (that is, the coordination number of Fe atoms) changes, thus causing local fluctuations of the strength of the various magnetic interactions. T_c, however, turns out to be sensitive to the average strength of the magnetic interactions over large distances rather than to the local fluctuations and thus is well defined. Notice that the lateral correlation length growing much larger than the film thickness is the key to observing a truly 2D phase transition.

Figure 3 shows a M versus t family of isochamps (curves with constant magnetic field). This figure shows the familiar picture $M(t)$ curves separating out according to the strength of the applied magnetic field. In agreement with the high value of the exponent δ, fields as small as 0.01 Oe (ref. 9) already introduce a measurable tail in the $M(t)$ curve. This strong response to minute magnetic fields is characteristic of 2D systems, for which $\delta = 15$ (ref. 11), and is not found in three-dimensional systems for which $\delta = 5$ (ref. 5).

The family of isochamps given in Fig. 3 collapses into just one single curve—the scaling function (that is, the equation of
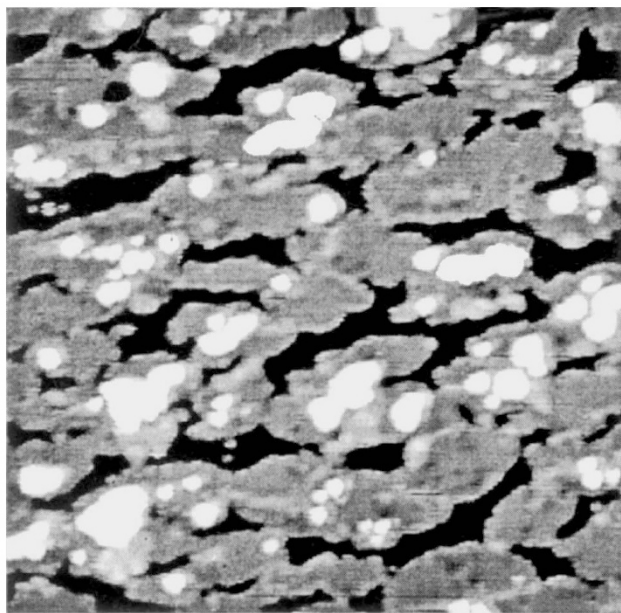

FIG. 1 STM topography of a 1.8 ± 0.1 AL of Fe on W(110). The image shows an area of 100×100 nm. The grey-scale range is 0.36 nm. Black corresponds to the first, grey to the second and white to the third Fe layer. A tunnelling current of 0.2 nA and a sample voltage of -620 mV were used to collect the image.
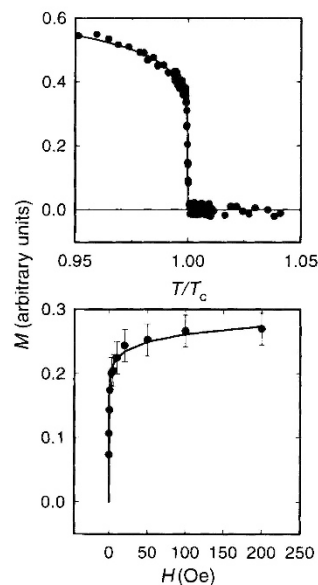

FIG. 2 Top, zero-field magnetization curve versus T/T_c ($H = 0 \pm 10$ mOe) measured using the magneto-optical Kerr effect for an Fe film 1.7 ± 0.1 AL thick. The thickness was determined from the STM topography. Absolute temperatures are determined to within ± 5 K, while relative temperatures are accurate to within 0.01 K. T_c (316.77 K in the present case) was determined separately, by locating the temperature at which $[M(T, H) - M(T, 0)]$ has a maximum[9], with a relative accuracy of ± 0.07 K. This means that the origin of the t-axis is known with an accuracy of $\pm 2 \times 10^{-4}$. The solid line is a power-law fit to the data $M \propto (1 - T/T_c)^\beta$ yielding $\beta = 0.13 \pm 0.02$. The error in β is due to the uncertainty in locating T_c. Bottom, magnetization as a function of the applied magnetic field at T_c. The solid line is a power-law fit to the data $M \propto H^{1/\delta}$, yielding $\delta = 14 \pm 5$. The critical isotherm was obtained by plotting the maximum value of the family of curves $[M(t, H) - M(t, 0)]$ versus H.

state in the critical region)—when the variables M and t are scaled by $H^{1/\delta}$ and $H^{1/\beta\delta}$, respectively[12] (Fig. 4a). This collapsing is a manifestation of the scaling hypothesis[1,12]. Except for a discrete number of data points on the left-hand side of the figure, deviation from scaling is <10%.

Whereas the representation of Fig. 4a—introduced by Hankey and Stanley[12]—is most suited to visualize the data-collapsing, plotting[13] $h(x) = H/M^\delta$ versus $x = t/M^{1/\beta}$ allows the determination of the zero-field susceptibility critical exponents γ and of the ratio of the critical amplitudes Γ_+/Γ_-, defined as $\chi(T) = \Gamma_+(t)^{-\gamma} (T > T_c)$ and $\chi(T) = \Gamma_- = \Gamma_-(-t)^{-\gamma} (T < T_c)$, see Fig. 4b. This representation of scaling is designated as the $h(x)$ representation of the scaling function[13]. For large x we expect the leading term[14] in $h(x)$ to be x^γ/Γ_+ (the point $(h(\infty), \infty)$ corresponds to the critical isochore). In this representation, the point $(h(x_0) = 0, x_0)$ corresponds to the zero-field magnetization curve shown in Fig. 2. In the vicinity of this point one expects[14] the leading term in $h(x)$ to be linear in $(x + x_0)$ with coefficient $\beta/\Gamma_- x_0^{(\gamma - 1)}$. The point $(h(0), 0)$ is the critical isotherm shown in Fig. 2. By fitting the measured scaling function in the corresponding ranges according to the expected functional form we obtain $\gamma = 1.74 \pm 0.05$ and $\Gamma_+/\Gamma_- = 40 \pm 10$. The theoretical 2D Ising values are $7/4$ (exactly known[15]) and $\Gamma_+/\Gamma_- \approx 37.7$ (ref. 16).

The coincidence between the measured critical quantities β, δ, γ, Γ_+/Γ_- and the calculated ones for the 2D Ising model might seem surprising at first sight. Our system is certainly not—see Fig. 1—the lattice with perfect translational symmetry underlying the Ising hamiltonian and the calculations by Gaunt and Domb[6]. Also Fe does not have localized spins as the Ising hamiltonian, which imitates rather an insulating ferromagnet with localized moments than a broad-band metallic ferromagnet like Fe. Moreover, although our uniaxial ferromagnet might
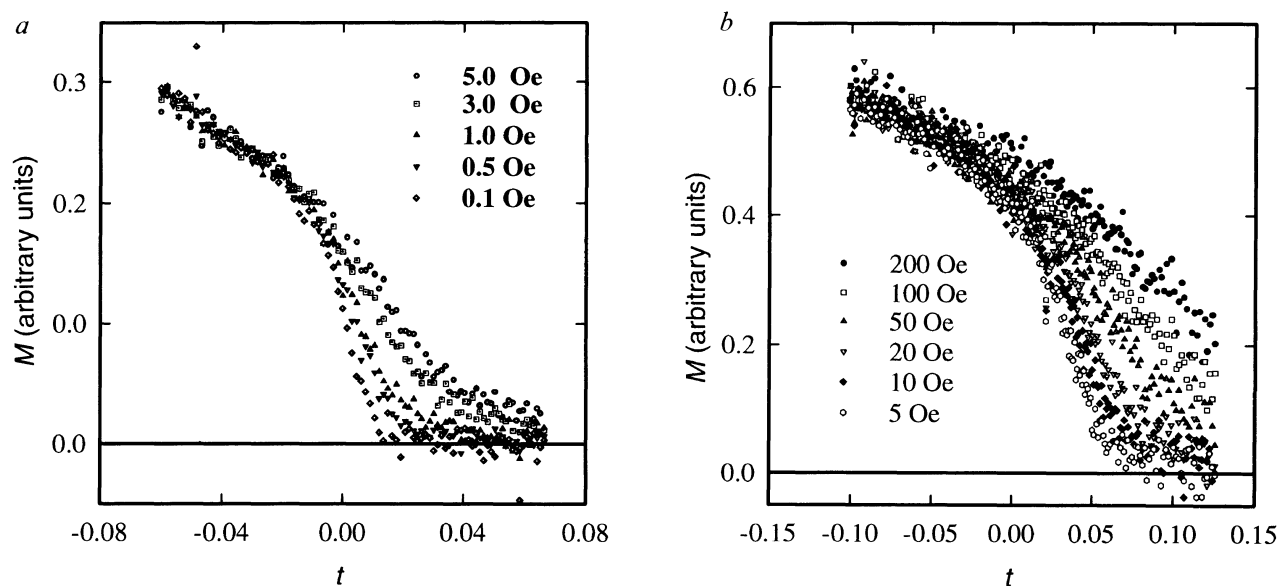
a

b

FIG. 3 Magnetization curves in constant magnetic field obtained in the vicinity of the Curie temperature as a function of t. For sample 1 (panel a) the applied field was varied between 0.1 and 5 Oe. For sample 2 (panel b) the field was varied between 5 and 200 Oe. The Curie temperatures were determined as in Fig. 2. The Curie temperature

of sample 1 was 331.3 K. Sample 2 was slightly thicker and had a Curie temperature of 345 K. Notice that in this thickness range (~1.7 AL) the phase transition occurs at temperatures close to deposition temperature, so the morphology does not change during the thermal scan.

have the same rotational symmetry as the 2D Ising hamiltonian, the strength of the various magnetic anisotropies in our films is very small (of the order of 1 K, compared to $T_c \approx 300$ K). Accordingly, the individual Fe-spins can move easily away from the easy axis and thus have more degrees of freedom than the Ising spins, which can only by 'up' or 'down'. In fact, the temperature dependence of the magnetization far away from the critical point deviates strongly from the 2D Ising behaviour (ref. 9). Finally, a realistic magnetic interaction between two Fe

spins $S_i S_j$ should be much more complicated than the scalar product (S_i, S_j) forthcoming in the Ising hamiltonian. Thus, the good agreement between the experimental and measured critical quantities should be regarded as a stringent test of the universality hypothesis[1,2]. According to this hypothesis, it is believed[14] that the critical exponents and the ratio of critical amplitudes depend only on (1) the spatial dimensionality of the system, (2) the number of components of the order parameter, (3) the symmetry of the hamiltonian and (4) the range of the micro-
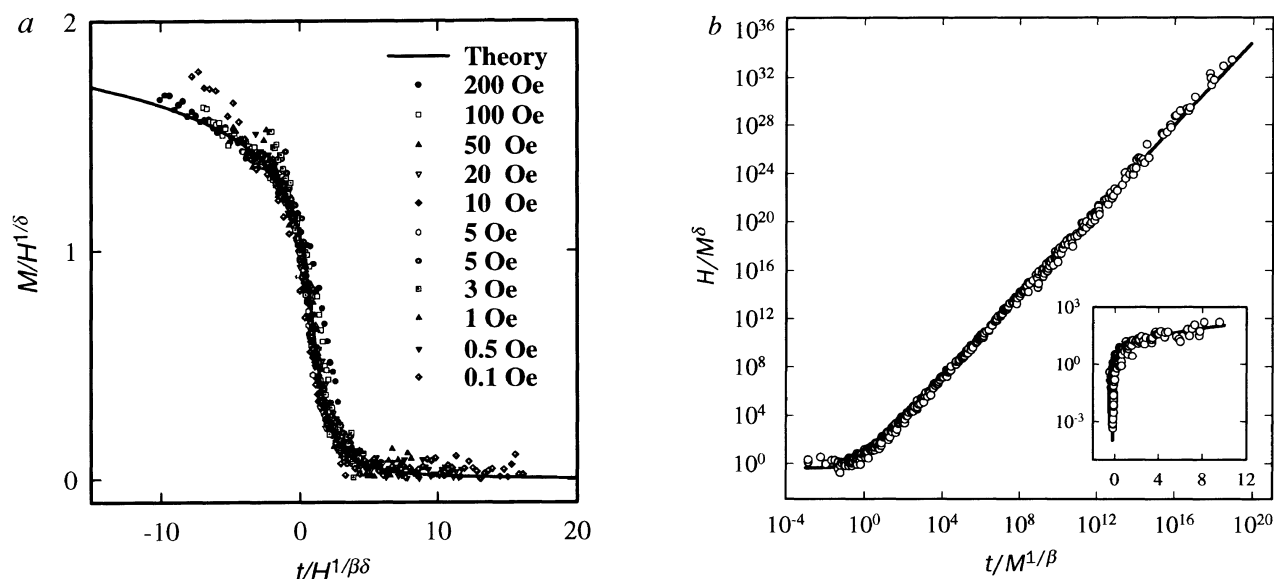
a

b

FIG. 4 a, Scaled magnetization $M/H^{1/\delta}$ versus scaled temperature $t/H^{1/\beta\delta}$ for the two films of Fig. 3. A linear scale is used. The solid line is the theoretical scaling function after ref. 6. For small fields, a discrete number of data points deviate from the scaling function. They are neglected in b. We used the value of β and δ determined from Fig. 2. For δ outside the range 12–16 the data collapsing is poorly realized.

This allows us to reduce the experimental uncertainty for δ to ± 2. b, Plot of H/M^δ versus $t/M^{1/\beta}$ for the two films of Fig. 3. The data with $x>0$ are represented as a log–log plot. The data points in the interval $-1 \times <10$ are represented semilogarithmically in the inset. The solid line is the theoretical curve from ref. 6. All data points, regardless of their value of H, are shown with the same symbol.

scopic interactions responsible for the phase transition. Also the presence of defects is expected to alter the universality class[14]. Apparently, the morphological defects observed in our system (Fig. 1) are not able to bring our system outside the Ising universality class. This might be related to the fact that such defects are not effective in limiting the correlation length.

A deeper level of universality was predicted[1,3,5,14]. At this level, provided that the non-universal scales for M and H are specified, the resulting scaling function should coincide within one universality class. This level of universality is also known historically as the Van der Waals Law of Corresponding States[4]: using properly normalized thermodynamic variables, all systems within the same universality class have the same equation of state. Thus, by suitably rescaling M and H (or, equivalently, $h(x)$ and x) it should be possible to bring the experimental scaling function and the theoretical one to coincidence. This rescaling is performed in Fig. 4, where the solid line is the theoretical scaling function of ref. 6 (the algebraic expressions used for constructing the solid lines in Fig. 4 are given explicitly in the Appendix of ref. 6). The theoretical and experimental results are normalized by the non-universal critical parameters $h(0)$ and x_0, as suggested in ref. 12. The agreement between the experimental scaling function and the calculated one extends over 18 orders of magnitude of the variable $x = t/M^{1/\beta}$.

The exact solution of the 2D Ising model in an applied magnetic field is still missing[2], so that one has to resort to approximate solutions. Our results confirm the validity of such calculations and represent a test of universality and scaling over a wide range of parameters. Further experimental work on this system along the lines of for example, refs 17–21 (including the experimental determination of the scaling behaviour of the correlation function[14] by, for example, a new generation of neutron spectrometers) should improve our knowledge of cooperative phenomena beyond the pure numerical awareness. □

1. Kadanoff, L. P. Physica A**163**, 1–14 (1990).
2. Baxter, R. J. Exactly Solved Models in Statistical Mechanics (Academic, London, 1982).
3. Levelt Sengers, A., Hocken, R. & Sengers, J. V. Physics Today **30**, 42–51 (1977).
4. De Boer, J. Physica **73**, 1–27 (1974).
5. Levelt Sengers, J. M. H. Physica **73**, 73–106 (1974).
6. Gaunt, D. S. & Domb, C. J. Phys. C**3**, 1442–1461 (1970).
7. Ising, E. Z. Phys. **31**, 253–258 (1925).
8. Kerkmann, D., Pescia, D. & Allenspach, R. Phys. Rev. Lett. **68**, 686–689 (1992).
9. Back, C. H., Würsch, C., Kerkmann, D. & Pescia, D. Z. Phys. B**96**, 1–3 (1994).
10. Yang, C. N. Phys. Rev. **85**, 808–816 (1952).
11. Domb, C. & Sykes, M. F. Proc. R. Soc. Lond. A **240**, 214–222 (1957).
12. Milosevic, S. & Stanley, H. E. in Rendiconti S. I. F., Course LIX (eds Müller, K. H. & Rigamonti, A.) (North-Holland, Amsterdam, 1976).
13. Griffiths, R. B. Phys. Rev. **158**, 176–87 (1967).
14. Kumar, A., Krishnamurthy, H. R. & Gopal, E. S. R. Phys. Rep. **98**, 57–143 (1983).
15. Abraham, D. B. Phys. Lett. **43A**, 163–164 (1973).
16. Barouch, E., McCoy, B. M. & Wu, T. T. Phys. Rev. Lett. **31**, 1409–1411 (1973).
17. Campuzano, J. C., Foster, M. S., Jennings, G., Willis, R. F. & Unertl, W. Phys. Rev. Lett. **54**, 2684–2687 (1985).
18. Qiu, Z. Q., Pearson, J. & Bader, S. D. Phys. Rev. Lett. **67**, 1646–1648 (1991).
19. Samuelsen, E. J. J. Phys. Chem. Solids **35**, 785–793 (1974).
20. Als-Nielsen, J., Birgenau, R. J., Guggenheim, H. J. & Shirane, G. Phys. Rev. B**12**, 4963–4979 (1975).
21. Birgenau, R. J., Guggenheim, H. J. & Shirane, G. Phys. Rev. B**8**, 304–311 (1973).

A 100-kyr periodicity in the flux of extraterrestrial ^{3}He to the sea floor

K. A. Farley & D. B. Patterson

Division of Geological and Planetary Sciences, MS 170-25, California Institute of Technology, Pasadena, California 91125, USA

MOST of the helium-3 in oceanic sediments comes from interplanetary dust particles (IDPs), and can therefore be used to infer the accretion rate of dust to the Earth through time[1-3]. ^{3}He records from slowly accumulating pelagic clays indicate that the accretion rate varies considerably over millions of years, probably owing to cometary and asteroidal break-up events[3]. Muller and MacDonald have proposed[4] that periodic changes in this accretion rate due to a previously unrecognized 100-kyr periodicity in the Earth's orbital inclination might account for the prominence of this frequency in climate records of the past million years[5]. Here we report variations in the ^{3}He flux to the sea floor that support this idea. We find that the flux recorded in rapidly accumulating Quaternary sediments from the Mid-Atlantic Ridge oscillates with a period of about 100 kyr. We cannot yet say, however, whether the 100-kyr climate cycle is a consequence of, a cause of, or an effect independent of these periodic changes in the rate of delivery of interplanetary dust to the sea floor.

The samples are from Deep Sea Drilling Project (DSDP) Site 607, on the flank of the Mid-Atlantic Ridge at 41° N. The core is a predominantly foraminiferal nanofossil ooze[6], and carries a continuous, high-sedimentation-rate record between 245 kyr and 1.6 Myr (ref. 6). Variations in δ^{18}O, δ^{13}C, $CaCO_3$ content and foraminifera populations in this core provide chronostratigraphic control and a detailed record of global climate conditions[8]. As with other climate records from deep-sea cores,

Site 607 demonstrates 23/19- and 41-kyr climate periodicities and the onset of 100-kyr glacial–interglacial cycling about 900 kyr ago. The 23/19- and 41-kyr periodicities can be attributed to precession and obliquity of the Earth's orbit, but the origin of the 100-kyr signal remains controversial[5]. Although variations in orbital eccentricity are of roughly the appropriate frequency[7], the resulting insolation modulation is insufficient to account for the observed climate record[5], nor is it clear why this signal first appeared about a million years ago. Identification of the origin of this cycle remains central to understanding Earth's climate system[5]. We have analysed the ^{3}He content of a complete 9-m section of core spanning 253 to 458 kyr to characterize the accretion rate of extraterrestrial matter over 10^5-year timescales and to investigate its possible relationship[4] to this 100-kyr climate periodicity.

Unlike previously studied sediments[1-3,9], this core is characterized by fairly low ^{3}He/^{4}He ratios of $\sim 2 \times 10^{-7}$ (Table 1), reflecting accumulation of ^{4}He-rich terrigenous material. Nevertheless, the ^{3}He/^{4}He ratios are nearly an order of magnitude higher than typical crustal matter, demonstrating the presence of an additional ^{3}He-rich component. To identify this ^{3}He source, we performed additional experiments on the samples. Magnetic separates were found to be highly enriched in ^{3}He and ^{3}He/^{4}He ratio (by up to 30 times over the bulk sediment), and stepped heating experiments further confirmed that ^{3}He and ^{4}He reside in different carriers. ^{4}He is overwhelmingly released at low temperatures (<500 °C), whereas ^{3}He has a bimodal release, at <500 °C and 950 °C. The high-temperature release (>600 °C) accounts for $\sim 75\%$ of the total ^{3}He. Helium release peaking at 950 °C and enrichment of ^{3}He in magnetic fines are the hallmark of IDP helium within sediments[10,11]. Using a simple deconvolution model that attributes the ^{3}He to crustal, atmospheric and extraterrestrial components, we calculate that in all samples, more than 75% of the ^{3}He is extraterrestrial (range 75–92%; Table 1). Replicate ^{3}He measurements have a typical standard deviation of 15%, far larger than our analytical uncertainty of $\sim 2\%$. This variablity is consistent with the presence of a rela-